A&A 598, A61 (2017)
DOI: 10.1051/0004-6361/201629509

Astronomy & Astrophysics

Resolving galaxy cluster gas properties at $z \sim 1$ with *XMM-Newton* and *Chandra*

I. Bartalucci[1], M. Arnaud[1], G. W. Pratt[1], J. Démoclès[1], R. F. J. van der Burg[1], and P. Mazzotta[2,3]

[1] Laboratoire AIM, IRFU Service d'Astrophysique – CEA DRF – CNRS – Université Paris Diderot, Bât. 709, CEA-Saclay, 91191 Gif-sur-Yvette Cedex, France
e-mail: iacopo.bartalucci@cea.fr
[2] Dipartimento di Fisica, Università di Roma Tor Vergata, via della Ricerca Scientifica 1, 00133 Roma, Italy
[3] Harvard-Smithsonian centre for Astrophysics, 60 Garden Street, Cambridge, MA 02138, USA

Received 10 August 2016 / Accepted 7 October 2016

ABSTRACT

Massive, high-redshift, galaxy clusters are useful laboratories to test cosmological models and to probe structure formation and evolution, but observations are challenging due to cosmological dimming and angular distance effects. Here we present a pilot X-ray study of the five most massive ($M_{500} > 5\times10^{14}\ M_{\odot}$), distant ($z \sim 1$), clusters detected via the Sunyaev-Zel'Dovich effect. We optimally combine *XMM-Newton* and *Chandra* X-ray observations by leveraging the throughput of *XMM-Newton* to obtain spatially-resolved spectroscopy, and the spatial resolution of *Chandra* to probe the bright inner parts and to detect embedded point sources. Capitalising on the excellent agreement in flux-related measurements, we present a new method to derive the density profiles, which are constrained in the centre by *Chandra* and in the outskirts by *XMM-Newton*. We show that the *Chandra-XMM-Newton* combination is fundamental for morphological analysis at these redshifts, the *Chandra* resolution being required to remove point source contamination, and the *XMM-Newton* sensitivity allowing higher significance detection of faint substructures. Measuring the morphology using images from both instruments, we found that the sample is dominated by dynamically disturbed objects. We use the combined *Chandra-XMM-Newton* density profiles and spatially-resolved temperature profiles to investigate thermodynamic quantities including entropy and pressure. From comparison of the scaled profiles with the local REXCESS sample, we find no significant departure from standard self-similar evolution, within the dispersion, at any radius, except for the entropy beyond 0.7 R_{500}. The baryon mass fraction tends towards the cosmic value, with a weaker dependence on mass than that observed in the local Universe. We make a comparison with the predictions from numerical simulations. The present pilot study demonstrates the utility and feasibility of spatially-resolved analysis of individual objects at high-redshift through the combination of *XMM-Newton* and *Chandra* observations. Observations of a larger sample will allow a fuller statistical analysis to be undertaken, in particular of the intrinsic scatter in the structural and scaling properties of the cluster population.

Key words. methods: data analysis – X-rays: galaxies: clusters – galaxies: clusters: intracluster medium

1. Introduction

High-mass, high-redshift galaxy clusters are of particular interest for a number of reasons. High-mass clusters are the ultimate examples of gravitational collapse, and so their evolution affords a unique probe of this process over cosmic time. Their abundance as a function of redshift is sensitive to the total matter content of the universe and its evolution, and their baryon fractions can be used as a distance indicator (Sasaki 1996; Pen 1997; Allen et al. 2004; and Mantz et al. 2014, for a recent application).

Clusters emit in the X-ray band via the thermal emission of the hot and rarefied plasma in the intracluster medium (ICM). This emission can be used to measure the density, temperature, and heavy-element abundances of the gas, properties that are fundamental for the characterisation of the plasma thermodynamics. Global properties integrated over the cluster extent, such as temperature T_X and the X-ray analogue of the Sunyaev-Zel'Dovich (SZ, Sunyaev & Zeldovich 1980) signal $Y_X = M_{gas}\times T_X$ (Kravtsov et al. 2006) can be used as proxies for the total mass. The analysis of radial profiles allows us to obtain measurements of the distribution of other fundamental thermodynamic quantities such as pressure and entropy. With the further assumption of hydrostatic equilibrium, the radial density and temperature distributions can be used to measure the total mass profile.

X-ray observations, though, are particularly challenging for high-redshift galaxy clusters. The X-ray flux suffers from cosmological dimming, $S_X \propto (1+z)^{-4}$, limiting the photon statistics. The challenge is even more pronounced in the cluster outskirts because of the steep density gradient in these regions. Furthermore, the small apparent size of clusters at high redshift (typically $\sim$1–2 arcmin radius), requires instruments with high spatial resolution to study the distribution of the emitting plasma.

Deep X-ray observations of high-mass, high-redshift objects are scarce in the literature. These objects are rare and thus difficult to find; furthermore, they are difficult to observe because of their intrinsic faintness in the X-ray band (see e.g. Rosati et al. 2009; Santos et al. 2012; Tozzi et al. 2015, for example). An alternative approach, pioneered by McDonald et al. (2014), consists of stacking a large number of shallow observations in order to derive the redshift evolution of the mean profiles. However, information on an individual cluster-by-cluster basis is necessarily lost in the stacking process. The determination of individual profiles allows the average profile to be determined and also,

crucially, the dispersion about it, thus linking the deviation from the mean to the (thermo-)dynamical history. This approach provides essential information on cluster physics (see e.g. the analysis of local REXCESS entropy profiles by Pratt et al. 2010), and is a key element for understanding the selection function of any survey. It is now clear that this function must be fully mastered in order to understand the properties of the underlying population, and for cosmological applications (e.g. Angulo et al. 2012). The selection function depends not only on global properties (i.e. the link between the observable and the mass and its dispersion), but also on the profile properties (e.g. more peaked clusters will have a higher luminosity; current SZ detection methods generally assume a certain pressure profile shape).

Here we present a new method to combine observations obtained with two current-generation X-ray observatories. *XMM-Newton* has the largest X-ray telescope effective area, ensuring sufficient photon statistics which helps to counterbalance the cosmological dimming. In turn, the high angular resolution of *Chandra* allows us to probe the inner parts of the cluster and to disentangle any point source emission from the extended cluster emission. Using this method, we characterise the ICM of the five most massive ($M_{500} > 5 \times 10^{14}\,M_{\odot}$)[1], distant ($z > 0.9$) clusters currently known. They have been detected via the SZ effect in the South Pole Telescope (SPT, Reichardt et al. 2013; Bleem et al. 2015) and *Planck* surveys (Planck Collaboration VIII 2011; Planck Collaboration XXXII 2015; Planck Collaboration XXVII 2016)[2]. For each object, we are able to make a quantitative measurement of the gas morphology and to determine the radial profiles for density, temperature, and related quantities (gas mass, pressure, and entropy).

Combining observations from the two observatories allows us to efficiently probe both the inner regions and the outskirts. The observation depth was optimised to be able to measure the temperature in an annulus around R_{500}, allowing us to quantitatively study the radial scatter out to this distance. We investigate evolution through comparison with the results based on the X-ray selected Representative *XMM-Newton* Cluster Structure Survey (REXCESS, Böhringer et al. 2007); in particular, we compare to the average and 1σ dispersion of the REXCESS density, temperature, pressure, and entropy profiles (Pratt et al. 2007, 2010; Croston et al. 2008; Arnaud et al. 2010). Our sample being SZ-selected, the comparison with REXCESS also allows us to address the question of X-ray versus SZ-selection in the high-mass, high-redshift regime. For a fair comparison with SZ-selected samples, we also compare to the stacked results of McDonald et al. (2014). Finally, to contrast with theory, we also compare our sample with the five most massive $z = 1$ clusters from the cosmo-OWLS numerical simulations of Le Brun et al. (2014).

The paper is organised as follows. In Sect. 2 we describe the *Chandra* and *XMM-Newton* sample used in our work and the procedures to clean and process the datasets. In Sect. 3 we present the analysis techniques used to perform the combination of the two instruments and to obtain radial profiles of density and 3D temperature, as well as the centroid shift used as dynamical indicator. In Sect. 4 we address the question of evolution in the profiles through comparison with REXCESS, and discuss the question of evolution. We compare our results with the high-redshift stacked entropy and pressure profiles of McDonald et al. (2014) and with the results of the numerical simulations of Le Brun et al. (2014) in Sects. 5 and 6, respectively. We then draw our conclusions in Sect. 7.

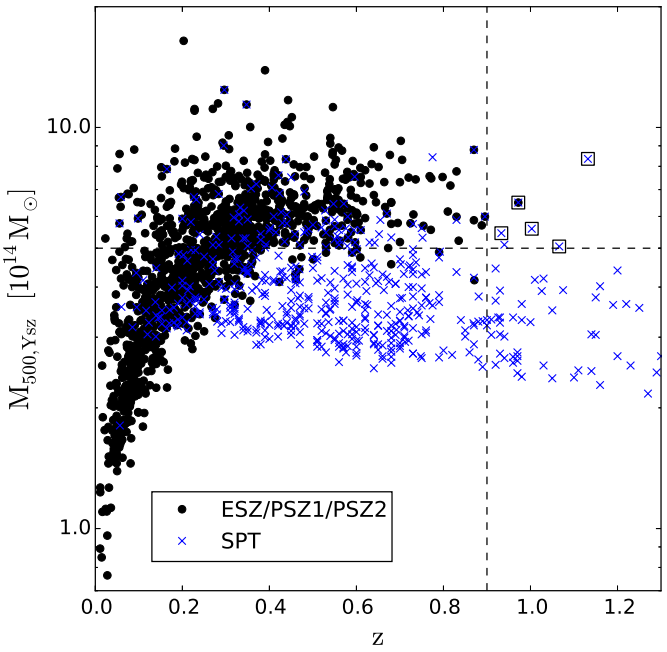

Fig. 1. Distribution of the galaxy clusters detected with *Planck* and SPT, denoted with black points and blue crosses, respectively. Dashed lines indicate the selection criteria defining our region of interest. Empty boxes highlight the 5 galaxy clusters forming our sample.

We adopt a flat Λ-cold dark matter cosmology with $\Omega_{\rm M} = 0.3$, $\Omega_{\Lambda} = 0.7$, $H_0 = 70\,{\rm km\,Mpc\,s^{-1}}$ and $h(z) = \sqrt{\Omega_{\rm m}(1+z)^3 + \Omega_{\Lambda}}$. All errors are shown at the 68 percent confidence (1σ) level. All the fitting procedures are performed using χ^2 minimisation.

2. Data preparation

2.1. Sample

Figure 1 shows all the confirmed clusters detected by the SPT and *Planck* surveys in the M–z plane. There are five clusters with $M_{500} > 5 \times 10^{14}\,M_{\odot}$ at $z > 0.9$, all of which were detected by SPT, and one, PLCK G266.6+27.3, was detected by both surveys. These are shown by black boxes in the figure.

We obtained an *XMM-Newton* Large Programme to observe four of these clusters in AO-13 (proposal 074440, PI M. Arnaud). The exposure times (typically 100 ks before cleaning) were tuned so as to obtain sufficient counts to extract high-quality spatially resolved temperature profiles up to R_{500}. The fifth cluster, PLCK G266.6+27.3, had already been observed to similar depth with *Chandra* (~225 ks, proposal 13800663, PI P. Mazzotta). In addition to our deep *XMM-Newton* data, the four SPT clusters had previously been observed as part of the *Chandra* X-Ray Visionary Project proposal 13800883 (P.I. B. Benson). Exposure times for these observations (typically 80 ks), were tuned so as to obtain ~2000 counts per cluster to allow for global properties to be measured (McDonald et al. 2014). The original ~25 ks snapshot observation of PLCK G266.6+27.3, obtained as part of the *Planck-XMM-Newton* validation programme, is described in Planck Collaboration XXVI (2011).

[1] M_{500} being the total mass of the cluster enclosed within R_{500}, which is the radius where the mean interior density is 500 times the critical density of the Universe.

[2] There are no clusters in this mass and redshift range in the Atacama Cosmology Telescope (ACT) survey (Marriage et al. 2011).

Table 1. The sample of the five galaxy clusters used in this work.

Cluster name	X-ray peak [J2000]	BCG [J2000]	$N_H{}^a$ [10^{20} cm^{-3}]	Redshift	XMM exp.^{b} [ks] M1 M2 PN	*Chandra* exp.^{c} [ks] ACIS	$\langle u \rangle$ [10^{-2} R_{500}] XMM *Chandra*	BCG X-ray peak distance [10^{-2} R_{500}]
SPT-CLJ 2146-4632	21 46 34.78 −46 32 54.06	21 46 34.57 −46 32 57.20	1.64	0.933	147.5 157.4 102.2	70.9	2.49 ± 0.17 2.46 ± 0.78	7.04
PLCKG266.6-27.3^d	06 15 51.83 −57 46 46.58	06 15 51.77 −57 46 48.61	4.32	0.972	11.4 12.4 2.9	226.7	0.68 ± 0.18 0.94 ± 0.11	1.62
SPT-CLJ 2341-5119	23 41 12.23 −51 19 43.05	23 41 12.37 −51 19 44.62	1.21	1.003	86.9 93.6 44.5	77.8	1.96 ± 0.16 2.98 ± 0.87	2.06
SPT-CLJ 0546-5345	05 46 37.22 −53 45 34.43	05 46 37.63 −53 45 30.49	6.79	1.066	126.0 127.9 112.9	67.9	1.16 ± 0.11 0.96 ± 0.34	5.63
SPT-CLJ 2106-5845	21 06 05.28 −58 44 31.70	21 06 04.60 −58 44 28.21	4.33	1.132	26.1 25.9 16.1	70.8	1.55 ± 0.21 1.90 ± 0.30	6.08

Notes. $^{(a)}$ The neutral hydrogen column density absorption along the line of sight is determined from the LAB survey (Kalberla et al. 2005). $^{(b,c)}$ We report the total exposure time after cleaning procedures. $^{(d)}$ SPT name: SPT-CLJ 0615-5746.

Observation details are given in Table 1. All the *XMM-Newton* observations were taken using the European Photon Imaging Camera (EPIC), combining the data taken with the MOS1, MOS2, and PN cameras. *Chandra* observations were taken using the Advanced CCD imaging spectrometer (ACIS, Garmire et al. 2003). *XMM-Newton* and *Chandra* images of all five objects are shown in Appendix A.

2.2. Data preparation

We processed *Chandra* observations using the *Chandra* Interactive Analysis of Observations (CIAO, Fruscione et al. 2006) ver. 4.7 and the calibration database[3] ver. 4.6.5. The latest version of calibration files were applied following the prescriptions detailed in `cxc.harvard.edu/ciao/guides/acis_data.html?` using the `chandra_repro` tool. To process the *XMM-Newton* datasets, we used the Science Analysis System[4] pipeline ver. 14.0 and calibration files as available in December 2015. New event files with the latest calibration applied were produced using the `emchain` and `epchain` tools.

2.3. Data filtering

We reduced the contamination from high-energy particles using the Very Faint Mode status bit[5] and the keyword PATTERN for the *Chandra* and *XMM-Newton* datasets, respectively. In particular, we removed from the analysis all the events for which the keyword PATTERN is <4 and <13 for MOS1, 2, and PN cameras. To remove periods of anomalous count rate, i.e. flares, we followed the prescriptions described in Markevitch's COOKBOOK[6] and Pratt et al. (2007) for *Chandra* and *XMM-Newton*, respectively. For both datasets, we extracted a light curve for each observation and removed from the analysis the time intervals where the count rate exceeds 3σ times the mean value. If there were multiple observations of the same objects, these were merged after the processing and cleaning procedures. We list in Table 1 the effective exposure times, after cleaning, for each instrument.

Point sources were identified using the CIAO `wavdetect` tool (Freeman et al. 2002) on [0.5−2], [2−8] and [0.5−8] keV exposure-corrected images. For *XMM-Newton* we ran Multiresolution wavelet software (Starck et al. 1998) on the exposure-corrected [0.3−2] keV and [2−5] keV images. We then inspected by eye each list to check for false detections and missed point sources. Within 3′ of the aimpoint of each *XMM-Newton* observation, we used the *Chandra* point source list as reference. The positions of point sources were compared and, in the case of missed or confused sources, we defined a circular region of 15″ radius to be used as a mask.

2.4. Background estimation

X-ray background emission can be separated into sky and instrumental components. The latter is the result of high-energy particles interacting with the detectors and with the telescope itself. To evaluate this component for *XMM-Newton*, we used filter wheel closed (Kuntz & Snowden 2008) datasets. For *Chandra*, we generated mock datasets using the analytical particle background model described in Bartalucci et al. (2014). We normalised these datasets based on the total count rates measured over the entire field of view in the [9.5−10.6] keV band for ACIS and [10−12], [12−14] keV for the MOS1-MOS2 and PN cameras, respectively. We then skycast the normalised instrumental datasets to match our observations and applied the same point source masking. In addition to the instrumental component, we also produced datasets reproducing out-of-time (OOT) events, following the prescriptions of Markevitch (2010) and using the SAS-`epchain` tool for *Chandra* and *XMM-Newton*. After skycasting and point source removal, we merged the OOT and instrumental datasets. From now on, we refer to this merge as "instrumental background datasets".

The sky background is due to a local component, formed by the Local Hot Bubble and the halo Galactic emission, and an extragalactic component (see, e.g., Snowden et al. 1995; Kuntz & Snowden 2000). The latter is the result of the superimposition of unresolved point sources, namely the cosmic X-ray background (CXB, Giacconi et al. 2001). In Sects. 3.2 and 3.4 below we describe in detail how we estimated and subtracted these components for imaging and for spectroscopic analysis.

2.5. Vignetting correction

We corrected for the vignetting effect following the method described in Arnaud et al. (2001), where we assigned a WEIGHT keyword to each detected event. This is defined as the ratio of the effective area at the aimpoint to the area at the event position (in detector coordinates) and energy. By doing so, the WEIGHT represents the effective number of photons we would detect if the instrument had the same response as at the aimpoint. To compute the WEIGHT we used the SAS `evigweight` tool and the procedures described in Bartalucci et al. (in prep.) for *XMM-Newton* and *Chandra*, respectively. For consistency, when subtracting the instrumental background, we also computed the WEIGHTs for the background datasets.

[3] `cxc.harvard.edu/caldb`
[4] `cosmos.esa.int/web/xmm-newton`
[5] `cxc.harvard.edu/cal/Acis/Cal_prods/vfbkgrnd`
[6] `cxc.harvard/contrib/maxim`

Table 2. Global properties.

Cluster	$T_X{}^a$ [keV]	$Y_X{}^b$ [$10^{14}\ M_\odot$ keV]	$R_{500}{}^c$ [kpc]	$M_{g500}{}^d$ [$10^{13}\ M_\odot$]	$M_{500,Y_X}{}^e$ [$10^{14}\ M_\odot$]
SPT-CLJ 2146-4632	$4.80^{+0.24}_{-0.21}$	$2.18^{+0.17}_{-0.16}$	$726.97^{+9.77}_{-11.10}$	$4.54^{+0.13}_{-0.14}$	$3.14^{+0.13}_{-0.14}$
PLCKG266.6-27.3	$11.04^{+0.56}_{-0.56}$	$13.42^{+1.00}_{-1.04}$	$1002.58^{+14.07}_{-14.38}$	$12.16^{+0.03}_{-0.03}$	$8.61^{+0.37}_{-0.37}$
SPT-CLJ 2341-5119	$7.08^{+0.36}_{-0.36}$	$3.72^{+0.27}_{-0.28}$	$777.65^{+10.66}_{-10.89}$	$5.26^{+0.12}_{-0.12}$	$4.17^{+0.17}_{-0.17}$
SPT-CLJ 0546-5345	$7.68^{+0.38}_{-0.33}$	$4.24^{+0.26}_{-0.30}$	$773.96^{+10.02}_{-8.94}$	$5.52^{+0.11}_{-0.10}$	$4.41^{+0.17}_{-0.15}$
SPT-CLJ 2106-5845	$10.04^{+0.83}_{-0.86}$	$10.08^{+1.10}_{-1.16}$	$882.94^{+18.20}_{-18.77}$	$10.10^{+0.31}_{-0.29}$	$7.07^{+0.45}_{-0.42}$

Notes. [(a)] Spectroscopic temperature measured in the $[0.15-0.75]\,R_{500}$ region. [(b)] Y_X is the product of $M_{gas,500}$ and T_X (Kravtsov et al. 2006). [(d)] The gas mass within R_{500}, derived using the combined density profiles. [(c,e)] R_{500} and M_{500,Y_X} are determined iteratively using the $M_{500}-Y_X$ relation of Arnaud et al. (2010), assuming self-similar evolution.

3. Radial profiles

All the techniques described in this section are applied to both the *Chandra* and *XMM-Newton* datasets, unless stated otherwise. Global cluster parameters are estimated self-consistently within R_{500} via iteration about the $M_{500}-Y_X$ relation of Arnaud et al. (2010), assuming self-similar evolution. The quantity Y_X is defined as the product of $M_{g,500}$, the gas mass within R_{500}, and T_X, the spectroscopic temperature measured in the $[0.15-0.75]\,R_{500}$ aperture. The X-ray properties of the clusters and resulting refined Y_X values are listed in Table 2.

3.1. X-ray peak and BCG positions

To assess how the choice of the centre affects our profiles, we used both the X-ray peak position and the brightest cluster galaxy (BCG) location as the centre for surface brightness and temperature profile extraction. Because of the higher spatial resolution, we determined the X-ray peak using *Chandra* images in the [0.5−2.5] keV band, smoothed using a Gaussian whose width ranges from three to five arcseconds. We determined the BCG positions on *Spitzer*/IRAC data taken from the archive (PID:60099, PID:70053, and PID:80012). If available (for all clusters except SPT-CLJ 2146-4632), positions were refined using archival HST imaging in the *F814W* band, which is part of HST programs 12246 and 12477. We give the positions in Table 1 and they are shown in the right column in Fig. A.1 by black and white crosses for the X-ray peak and BCG position, respectively.

3.2. Surface brightness profiles

We extracted vignetting-corrected and instrumental-background-subtracted surface brightness profiles from *XMM-Newton* datasets using concentric annuli in the [0.3−2] keV band, each annulus being 3.3″ wide. For *Chandra* datasets we extracted the profiles in the [0.7−2.5] keV band, each annulus being 2″ wide. We evaluated the sky background component in a region free from cluster emission, i.e. where the instrumental background-subtracted surface brightness profiles flatten. Sky background subtracted surface brightness profiles were then binned to have a significance of at least 3σ per bin.

3.3. Density profiles

Density profiles were determined by applying deprojection with the regularisation technique described in Croston et al. (2006). Briefly, from the surface brightness profiles we produced PSF-corrected and deprojected emission profiles. For *XMM-Newton* we used the PSF parametrisation described in Ghizzardi (2001), while for *Chandra* we assumed a perfect PSF and only account for geometrical deprojection. We converted the emission measure profiles to gas density using a factor that depends on temperature and redshift, namely $\lambda(T, z)$. As already pointed by several works, there is a mismatch between temperatures measured by *Chandra* and *XMM-Newton*: on average, *XMM-Newton* temperatures are ∼15% lower than those of *Chandra* at 10 keV. However, as discussed in Bartalucci et al. (in prep.), the conversion factor is only weakly dependent on the temperature so that the offset between the two instruments is negligible for the computation of the density profiles. The conversion factors for *Chandra* and *XMM-Newton* were computed using their respective temperature profiles and assuming an average abundance of $0.3\ Z_\odot$. If we did not have a temperature profile (see below), we used the global temperature T_X listed in Table 2 to obtain the conversion factor. Using a conversion factor evaluated via a spatially resolved temperature or a single global value results in a negligible difference in the final density profile[7].

Figure 2 shows the deprojected density profiles computed from *XMM-Newton* and *Chandra* with blue and orange rectangles, respectively, using the X-ray peak as centre. The profiles are scaled by $h(z)^{-2}$ to account for self-similar evolution (Croston et al. 2008). The corresponding BCG-centred profiles are shown in Fig. B.1.

3.4. Temperature profiles

3.4.1. Temperature profile extraction

To measure the projected 2D temperature profiles, we analysed the spectra extracted from concentric annuli centred on the X-ray peak, each bin width being defined to have at least a signal-to-noise ratio of 30σ above the background level in the [0.3−2] keV and in the [0.7−2.5] keV band for *XMM-Newton* and *Chandra*, respectively. Spectra were binned to have at least 25 counts per energy bin after instrumental background subtraction. Following these prescriptions, we were able to define at least four annuli in all *XMM-Newton* datasets except for PLCK G266.6+27.3, where the deep *Chandra* observation allowed us to define seven annuli.

[7] Temperature profiles typically vary by ∼30% (Vikhlinin et al. 2006; Pratt et al. 2007; Arnaud et al. 2010). However, these variations induce only ∼1% effects on the resulting density profile, thus any difference in the radial temperature profile as measured by *XMM-Newton* and *Chandra* (e.g. Donahue et al. 2014) would have a similarly negligible effect.

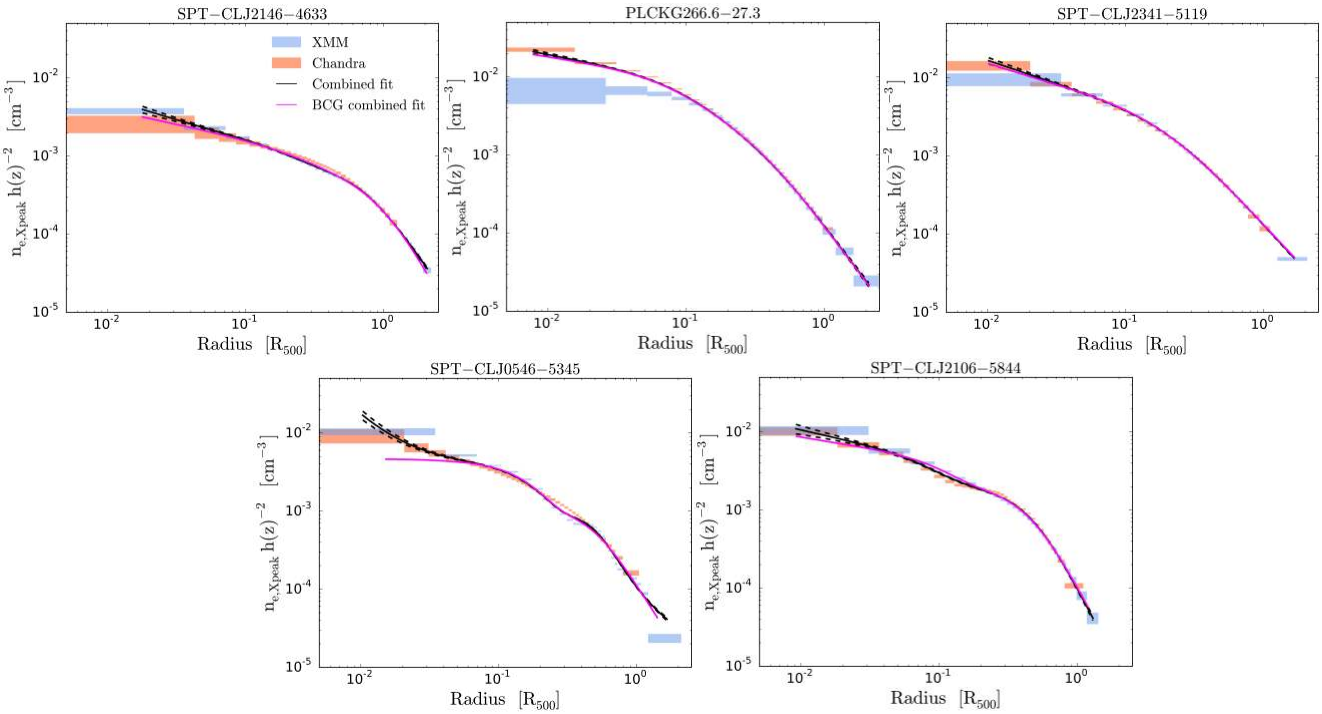

Fig. 2. Normalised, scaled, deprojected, density profiles centred on the X-ray peak. Blue and orange rectangles represent *XMM-Newton* and *Chandra* datasets, respectively. The solid black line shows the combined density profile resulting from the simultaneous fit to the *XMM-Newton* and *Chandra* data, as discussed in the text. Its uncertainties are shown with the dashed line. The magenta line shows the simultaneous fit for the profiles centred on the BCG.

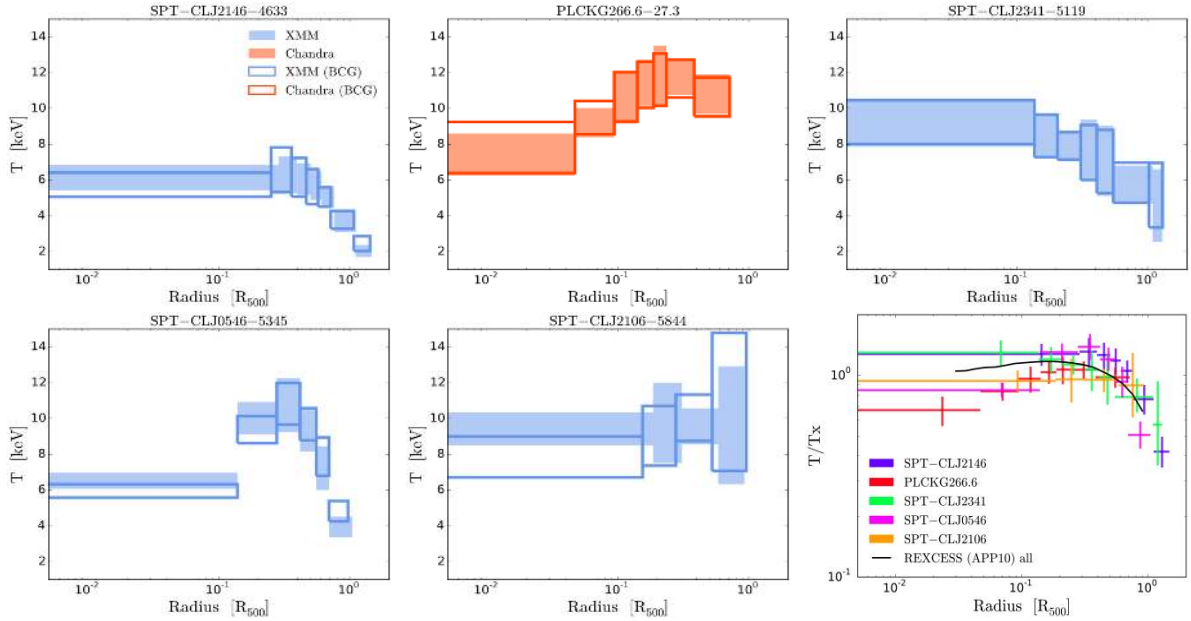

Fig. 3. *First five panels*: 3D temperature profiles. Blue and orange rectangles are profiles determined using *XMM-Newton* and *Chandra* datasets, respectively. Filled and empty boxes represent profiles computed using the X-ray peak and the BCG as centre, respectively. *Bottom right panel*: 3D X-ray peak-centred temperature profiles scaled to their global T_X values. The solid black line shows the average value of the REXCESS temperature profiles (Pratt et al. 2007; Arnaud et al. 2010, APP10). Profiles are colour coded according to the mass estimated from M_{500,Y_X}, the most massive being red and least massive being blue.

For the other four clusters, the *Chandra* observations were not deep enough to determine a temperature radial profile. For this reason, from now on all the temperature-based quantities for PLCK G266.6+27.3 are computed using the *Chandra* dataset, while for the others we use the *XMM-Newton* observations.

Our spectroscopic analysis consists of a spectral fit using a combination of models accounting for the cluster and sky background emission. We modelled the latter using two absorbed MEKAL models (Mewe et al. 1985, 1986; Kaastra 1992; Liedahl et al. 1995) plus an absorbed power law with index fixed

to 1.42 (Lumb et al. 2002) to account for the Galactic and the CXB emission, respectively. For one of the MEKAL models, the absorption was fixed to 0.7×10^{20} cm^{-3}; for the other two models the absorption was fixed to the Galactic value along the line of sight, as listed in Table 1. The absorption was accounted for in the fit by using the WABS model (Morrison & McCammon 1983). To estimate the sky background normalisations and temperatures, the model was fitted to a spectrum that was extracted from a region that is free of cluster emission, vignetting-corrected, and instrumental-background-subtracted. Once determined, we fixed these sky background models and simply scaled them by the ratio of the areas of the extraction regions. We modelled the cluster emission using an absorbed MEKAL whose absorption was fixed to the values given in Table 1. From the fit of this component we then determined the normalisation and the temperature. The photon statistics of the sample did not allow us to measure the abundances with an error lower than 30%, so we fixed the abundance to 0.3 $Z_\odot$. Fitting was undertaken in XSPEC[8] using the [0.3−11] keV and [0.7−10] keV range for *XMM-Newton* and *Chandra*, respectively. To avoid prominent line contamination in the *XMM-Newton* data, we excluded the [1.4−1.6] keV spectral range for all three camera datasets and the [7.45−9.0] keV band for PN only (see e.g. Pratt et al. 2007). We convolved all the models by the appropriate response matrix file (RMF), which were computed using the SAS `rmfgen` and the CIAO `mkacisrmf` tools. Convolved models were then multiplied by the ancillary response file computed at the aimpoint using the SAS `arfgen` and the CIAO `mkarf` tools.

3.4.2. 3D temperature profiles

We determined the 3D temperature profiles by fitting a parametric model similar to that described in Vikhlinin et al. (2006) to the 2D profiles. The models were convolved with a response matrix that simultaneously takes into account projection and PSF redistribution (the latter being set to zero for the *Chandra* data). In convolving the models, the weighting scheme introduced by Vikhlinin (2006; see also Mazzotta et al. 2004) was used to correct for the bias introduced by fitting isothermal models to a multi-temperature plasma. We computed the uncertainties via Monte Carlo simulations of 1000 random Gaussian realisations of the projected temperature profiles.

Using a parametric model may over-constrain the resulting temperature profile and hence underestimate the error. For this reason, if the resulting error in a specific bin was smaller than the one in the 2D profiles we used the latter as the final error. The 3D *XMM-Newton* and *Chandra* temperature profiles are shown with blue and orange rectangles, respectively, in Fig. 3. The empty boxes show the profiles obtained when centring the annuli on the BCG. The two profiles are consistent within the uncertainties for all objects.

3.4.3. Effect of the PSF on T_X

The value of T_X derived from the *XMM-Newton* spectrum in the projected [0.15–0.75] R_{500} radial range was not corrected for the PSF. At these redshifts, 0.15 R_{500} is about 15 arcsec, comparable to the size of the PSF. Redistribution of photons from the cluster core to the aperture in question could bias T_X, although we expect the effect to be small, since the temperature profiles are rather flat in the cluster centre and no density profile is particularly peaked. To quantify the effect, we computed

[8] heasarc.gsfc.nasa.gov/xanadu/xspec/

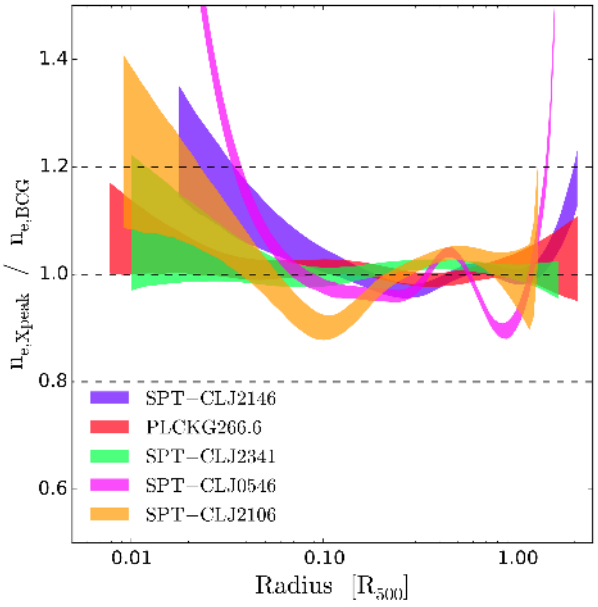

Fig. 4. Ratio between the combined density profiles centred on the X-ray peak and those centred on the BCG. The colour scheme is the same as in the bottom right panel of Fig. 3.

the spectroscopic-like temperature in the [0.15–0.75] R_{500} aperture using the best-fitting convolved temperature profile model, with and without taking into account the *XMM-Newton* PSF. We first checked that the value derived taking into account the PSF, $T_{sl,psf}$, is consistent with the directly measured T_X values for each cluster within the error bars. The median ratio is 1.03. We then compared this spectroscopic-like temperature, $T_{sl,psf}$, with that obtained without taking into account the PSF, i.e. the model value for a perfect instrument. The difference is 1% on average. The effect of the PSF is indeed negligible on T_X.

3.5. Chandra XMM combination

As shown in Figs. 2 and B.1, there is excellent agreement between the deprojected *Chandra* and *XMM-Newton* density profiles beyond ∼0.1 R_{500}. The two profiles contain complementary information. The higher effective area of *XMM-Newton* constrains the density profiles up to ∼1.5 R_{500} in all cases. Furthermore, the higher photon statistics are fundamental to clearly detect the presence of substructure, such as the "knee" features in the density profiles of SPT-CLJ 0546-5345 and SPT-CLJ 2106-5845. Conversely, the higher *Chandra* resolution is useful to probe the inner regions, where the radial binning of the profile can be finer than that of *XMM-Newton*. We thus combined the two deprojected density profiles by undertaking a simultaneous fit with a parametric modified beta model similar to that described in Vikhlinin et al. (2006). The resulting fit is a smooth and regular function, that can be easily integrated or differentiated, which at the same time efficiently combines information from the two instruments. As discussed in Bartalucci et al. (in prep.), *Chandra* and *XMM-Newton* density profile shapes are in good agreement with a normalisation offset of the order of 1%. For this reason, during the simultaneous fit we added a normalisation factor accounting for this effect as a free parameter. Errors were computed by performing 1000 Monte Carlo realisations of the simultaneous fit of the deprojected density profiles. The improvement due to the instrument combination is evident in Figs. 2 and B.1, where we show the combined parametric

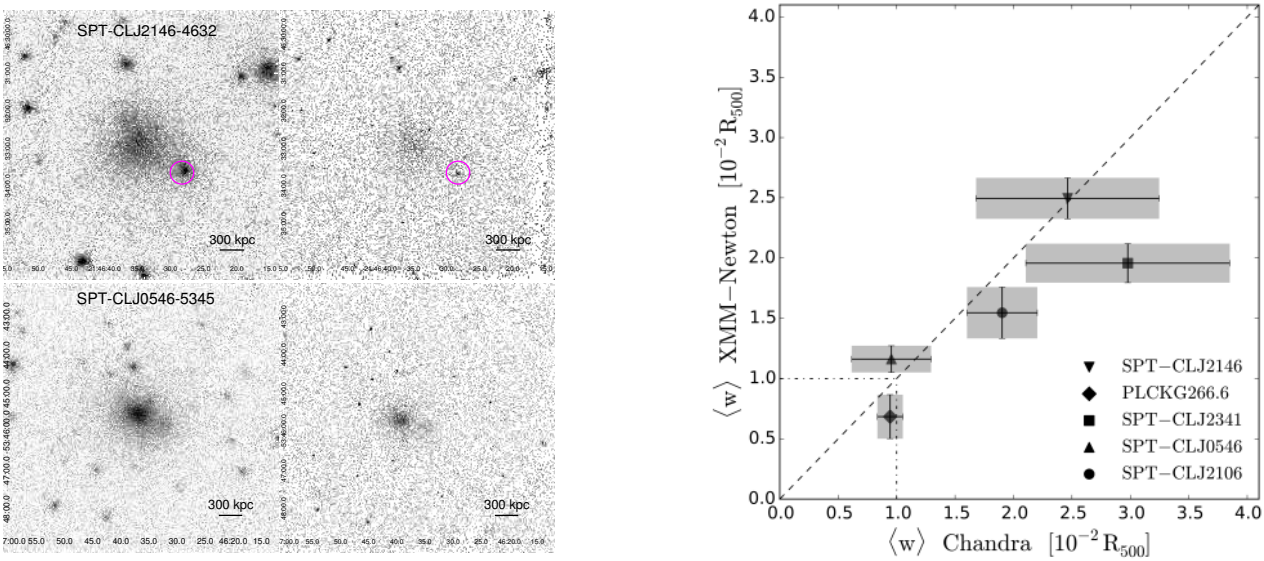

Fig. 5. *Left panel*: *XMM-Newton* (*left*) and *Chandra* (*right*) images of SPT-CLJ 2146-4632 (*top*) and SPT-CLJ 0546-5345 (*bottom*) in the [0.3−2] keV band. The images pixel size is 2″, and for ease of comparison, the same scale is used for all. The magenta circle identifies the point source that contaminates the substructure emission in the *XMM-Newton* image of SPT-CLJ 2146-4632. *Right panel*: centroid shift parameter, $\langle w \rangle$, values computed using *Chandra* and *XMM-Newton* in units of $10^{-2}\,R_{500}$. The dashed line is the identity relation. The two dot-dashed lines define the region where the clusters are considered to be dynamically relaxed (see text).

density profile and associated errors with solid and dotted black lines, respectively. In all cases the resulting profiles are well constrained at large radii with the *XMM-Newton* datasets, whereas in the central regions *Chandra* drives the fit. The combined profiles also retain information on the presence of features such as the knee observed in the *XMM-Newton* profile of SPT-CLJ 0546-5345, shown in Fig. 2.

The density profiles of PLCK G266.6+27.3 exhibit strong disagreement between the two instruments in the inner region, independent of whether the profile is centred on the X-ray peak or the BCG. The *Chandra* image in the right column of Fig. A.1 shows that the cluster emission in the core presents a complex structure. Taking the BCG as reference, there is a small region of low surface brightness emission to the north-west and a horseshoe-like region of high surface brightness emission around it to the north. The typical scale of these features is of ∼4″, so that the different resolving power of the instruments can significantly change the apparent emission distribution in these inner regions.

The accuracy of the combined profile in the inner parts allows us to study the impact of the choice of the centre. We repeated the same analysis for the density profiles centred on the BCG position and show the combined profiles with a black line in Fig. B.1. For comparison, BCG (X-ray-peak) centred profiles are shown in Fig. 2 (Fig. B.1) with magenta lines. As expected, BCG-centred profiles are shallower in the inner parts, but exhibit similar behaviour to the X-ray peak-centred profiles beyond $0.1\,R_{500}$. Figure 4 shows the ratio of X-ray peak- to BCG-centred profiles. As expected, the clusters for which the difference between the X-ray peak and the BCG positions are larger (notably SPT-CLJ 2146-4632, SPT-CLJ 0546-5345, and SPT-CLJ 2106-5845) exhibit more variation between profiles in the core. The choice of centre thus appears to affect the inner parts of the profiles, but does not seem to affect the outer part.

In the following we use the combined density profiles to perform our study and to derive all the other quantities.

3.6. Morphological analysis

We adopted the centroid shift value introduced by Mohr et al. (1993), namely $\langle w \rangle$, as an objective estimator of the morphological state of the cluster. The centroid shift is defined as the standard deviation of the projected distance between the X-ray peak and the centroid, measured in concentric circular apertures. To compute $\langle w \rangle$ we followed the implementation described in Maughan et al. (2008). Briefly, the centroids were measured on exposure-corrected and background-subtracted images in the [0.3−2] keV and [0.5−2.5] keV bands, for *XMM-Newton* and *Chandra*, respectively. To enhance the sensitivity to faint substructures, we masked the contribution in the inner region of the cluster and computed the centroid in ten concentric annuli in the range $[0.1-1]\,R_{500}$. Images were binned using the same pixel size of 2″. To test the dependence of $\langle w \rangle$ on image resolution, we repeated the same analysis on *Chandra* images binned with a pixel size of 1″. We found consistent results within the 1σ error bar. We computed the error by undertaking 100 Poisson realisations of the image and taking the 1σ standard deviation of the resulting $\langle w \rangle$ distribution. Values for $\langle w \rangle$ are listed in units of $10^{-2}\,R_{500}$ in Table 1.

The right panel of Fig. 5 shows the comparison between the $\langle w \rangle$ as computed using *XMM-Newton* and *Chandra*. Dot-dashed lines highlight the region of relaxed clusters, $\langle w \rangle < 0.01$, as defined for the REXCESS sample (Pratt et al. 2009). There is good agreement between the measurements, $\langle w \rangle$ being consistent at 1σ in all cases. However, for a given exposure time, the higher photon statistics of the *XMM-Newton* observations yield typically ∼3 times smaller uncertainties. This can be important for the classification of objects as relaxed or otherwise (see e.g. SPT-CLJ 0546-5345 in Fig. 5).

The left panel of Fig. 5 shows example *XMM-Newton* and *Chandra* images of SPT-CLJ 2146-4632 and SPT-CLJ 0546-5345 in the [0.3−2] keV band. They have been background subtracted and corrected for exposure time and are shown on exactly the same scale. Substructures are highlighted with blue dotted circles in the *XMM-Newton* images in Fig. A.1. In the

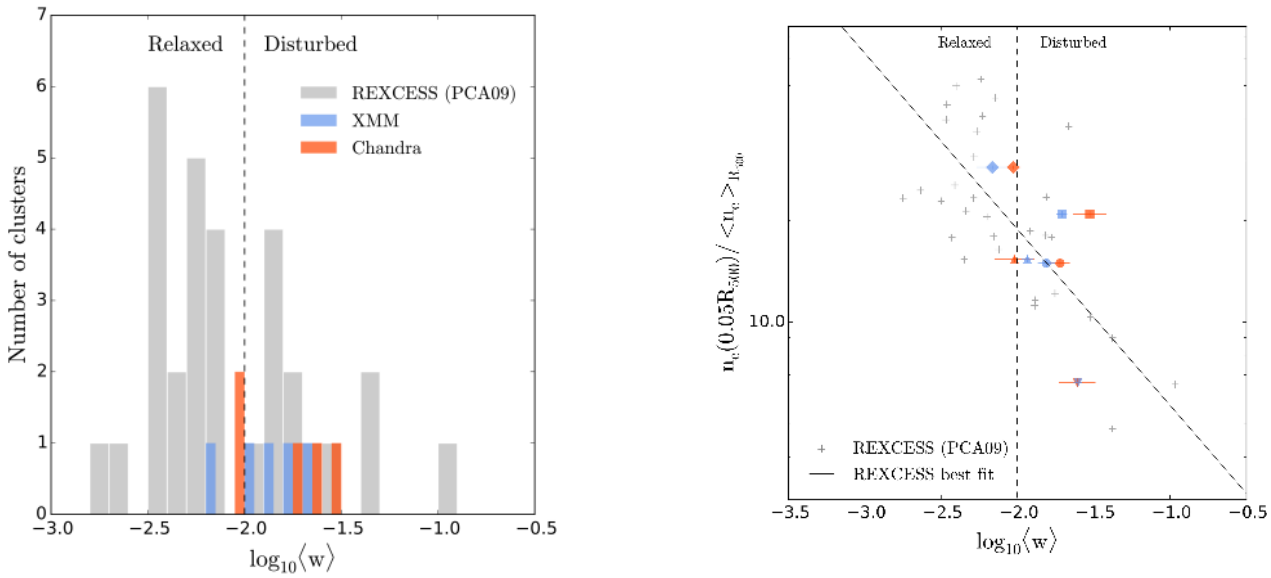

Fig. 6. *Left panel*: number of clusters as a function of $\langle w \rangle$ for the REXCESS sample (Pratt et al. 2009, PCA09) are plotted in grey. Our objects are plotted in blue and red for *XMM-Newton* and *Chandra*, respectively. The dashed line separates morphologically disturbed clusters from the rest. We plot *XMM-Newton* and *Chandra* lines using a binsize of 0.05 for clarity reasons, whereas for the histogram computation we use a binsize of 0.1. *Right panel*: distribution of the scaled density computed at 0.05 R_{500} as a function of $\langle w \rangle$. Grey crosses show the REXCESS sample, while blue and red points represent *XMM-Newton* and *Chandra* measurements, respectively, of our sample. The black solid line is the best-fit of the REXCESS sample.

case of SPT-CLJ 0546-5345 the substructure at $\sim 0.4\,R_{500}$ in the south-west sector is detected at much higher significance with *XMM-Newton* allowing unambiguous classification of its dynamical state. *XMM-Newton* clearly detects diffuse emission at $\sim 0.9\,R_{500}$ in the south-west sector of SPT-CLJ 2146-4632, to which the $\langle w \rangle$ is sensitive. However, this emission also contains some contribution from a point source, highlighted with a magenta circle in Fig. 5. The *Chandra* image allows us to accurately determine the point source location, and hence mask it properly in the *XMM-Newton* image. It is important to note that a complete morphological analysis of high-redshift clusters thus needs both instruments to efficiently detect faint diffuse emission and to account for point source contamination.

4. Evolution of cluster properties

4.1. Dynamical status

Figure 6 compares the $\langle w \rangle$ distribution of REXCESS (Pratt et al. 2009) and our sample. Taking the centroid shift values from *XMM-Newton* as a baseline, we find that our sample is dominated by disturbed clusters using the REXCESS definition ($\langle w \rangle > 0.01$). Only PLCK G266.6+27.3 appears relaxed, confirming the initial results of Planck Collaboration XXVI (2011). This result is expected from structure formation theory, in which the merging rate at high redshift is higher than in the local universe (see e.g. Gottlöber et al. 2001; or Hopkins et al. 2010).

In the following, we compare scaled profiles considering both the full REXCESS sample and the subsample composed only of the dynamically disturbed REXCESS clusters.

4.2. Scaled density and gas-mass profiles

The global cluster properties computed from the M_{500}–Y_X relation, assuming self-similar evolution, are given in Table 2, together with the details of the computation. The left panel of Fig. 7 shows the density profiles scaled to the average density integrated within R_{500}. The profiles are colour-coded based on their temperature T_X, as reported in Table 2, where blue is 4 keV and red is 14 keV. We also show the 1σ dispersion of the full REXCESS sample, and the subset of morphologically disturbed REXCESS clusters using golden and green envelopes, respectively. For a reference value, we fit the full REXCESS sample using an AB model (see Pratt & Arnaud 2002), and this is shown with a black dotted line. The profiles are, on average, in good agreement within the REXCESS scatter, but below the average reference value. This is not the case considering only disturbed clusters, where our sample is in excellent agreement within the scatter. The right panel of Fig. 6 shows the scaled density computed at 0.05 R_{500} as a function of $\langle w \rangle$. The centroid shifts computed using *Chandra* and *XMM-Newton* are plotted in red and blue, respectively. The majority of our sample has a large $\langle w \rangle$ and a flatter central density, and thus these objects lie in the parameter space of disturbed clusters. We suggest that there is no evident sign of evolution in the density profile shape, apart from that related to the evolution of the dynamical state. The profile of SPT-CLJ2146-4632, shown with the blue line in Fig. 7, lies outside the REXCESS 1σ envelope. We are not able to asses whether the difference is due to a particular behaviour, for instance related to its (relatively) very cool temperature, or if it is truly an outlier. Interestingly, we also identify a similar outlier in the simulated dataset (see below).

From the density profiles we compute the gas-mass profiles by integrating in spherical shells. These are shown in Fig. 7, where the dimensionless gas-mass profiles are scaled to the value integrated within R_{500}. There is good agreement between our sample and REXCESS. Furthermore, as discussed in Croston et al. (2008), we find the same behaviour of the gas mass as a function of temperature: hotter clusters have a larger gas fraction within R_{500}.

We compute the same quantities using the profiles centred on the BCG and we find the same results.

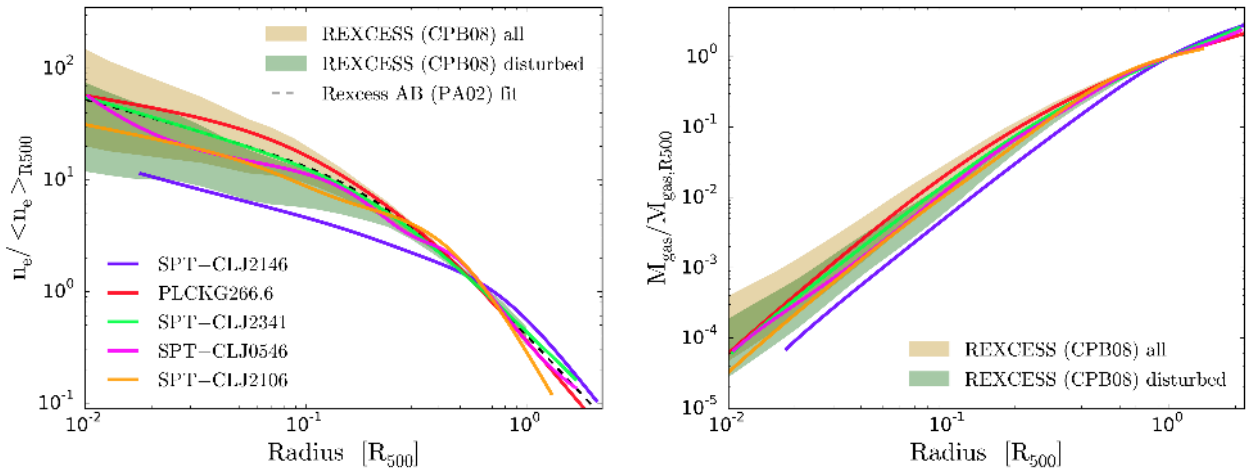

Fig. 7. *Left panel*: density profiles scaled by the integrated density within R_{500}. Gold and green shaded areas are the scatter computed from REXCESS density profiles (Croston et al. 2008, CPB08) using the full sample and only the disturbed objects (Pratt et al. 2009), respectively. The dashed line is the fit of the average REXCESS density profile with an AB model (Pratt & Arnaud 2002, PA02). The profile colour-coding is the same as in the bottom right panel of Fig. 3. *Right panel*: gas mass profiles scaled to the average gas mass within R_{500}. The colour-code is same as in the left panel.

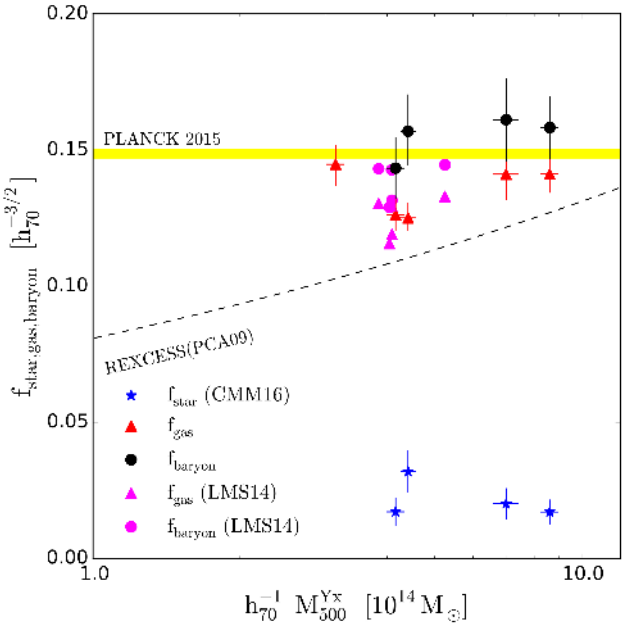

Fig. 8. Fraction of mass in stars, gas and total baryons at R_{500}. Blue stars and red triangles represent the stellar mass fraction (Chiu et al. 2016, CMM16) and the gas-mass fraction at R_{500}, respectively. The black points represent the sum of the two (i.e. the total baryon mass). For SPT-CLJ2 146-4632 there are no stellar mass fraction measures available. Magenta points show the gas and total baryon fraction of five clusters with $M_{500} > 4.5 \times 10^{14}\ M_\odot$ from the cosmo-OWLs simulations (Le Brun et al. 2014, LMS14). The yellow area is the baryon fraction as measured from Planck Collaboration XIII (2016). The dashed black line is the variation of gas-mass fraction with mass in the REXCESS sample (Pratt et al. 2009, PCA09).

4.3. Baryon content

One of the open issues related to the mass content of galaxy clusters is the evolution of the baryon fraction, defined as the ratio of stellar plus ICM content to the total cluster mass. To estimate the total baryon fraction for our sample we use the stellar mass computed by Chiu et al. (2016), who computed the stellar mass for 14 SPT clusters, four of which are in common with our sample. (The stellar mass is not available for SPT-CLJ 2146-4632.) Figure 8 shows the stellar, gas, and total baryonic mass fraction at R_{500}. We also plot the best-fit REXCESS gas mass fraction versus total mass relation (Pratt et al. 2009). While our sample is small and the scatter of the REXCESS fit is large, the gas-mass fractions of the four clusters in the present sample lie above the local reference; in addition, there does not appear to be a variation of gas or baryon fraction with mass. The total baryon fractions of the four clusters for which we have measurements are all in agreement with the cosmic baryon fraction measured by Planck Collaboration XIII (2016).

4.4. Thermodynamical profiles

Pressure and entropy profiles are computed using the density and temperature profiles described in the preceding sections. Since the radial sampling of the density profiles is finer, we interpolate them to match the radial binning of the temperature profiles. Typically we have five temperature profile bins, but in the following plots we show solid continuous lines to guide the eye.

4.4.1. Pressure profiles

As discussed in Arnaud et al. (2010), pressure profiles typically exhibit a smaller dispersion than the other quantities because of the anti-correlation between density and temperature. The left panel of Fig. 9 shows the pressure profiles scaled by P_{500}, and by the factor $f(M) = (M_{500}/3 \times 10^{14}\ h_{70}^{-1}\ M_\odot)^{0.12}$ to account for the mass dependency (see Eq. (10) of Arnaud et al. 2010). We also show the 1σ REXCESS envelopes for the full sample and the disturbed subsample, and the universal pressure profile from Arnaud et al. (2010). To better visualise the behaviour in the central parts, we also show the pressure profiles extrapolated assuming a flat temperature profile in the core. Our scaled profiles are in excellent agreement with REXCESS over the entire radial range, considering both the full sample and the disturbed subsample. Interestingly, there is a very small scatter above ~0.2 R_{500}. As with the density, the pressure profile of SPT-CLJ2146-4632 deviates significantly from the others, lying outside the REXCESS envelopes.

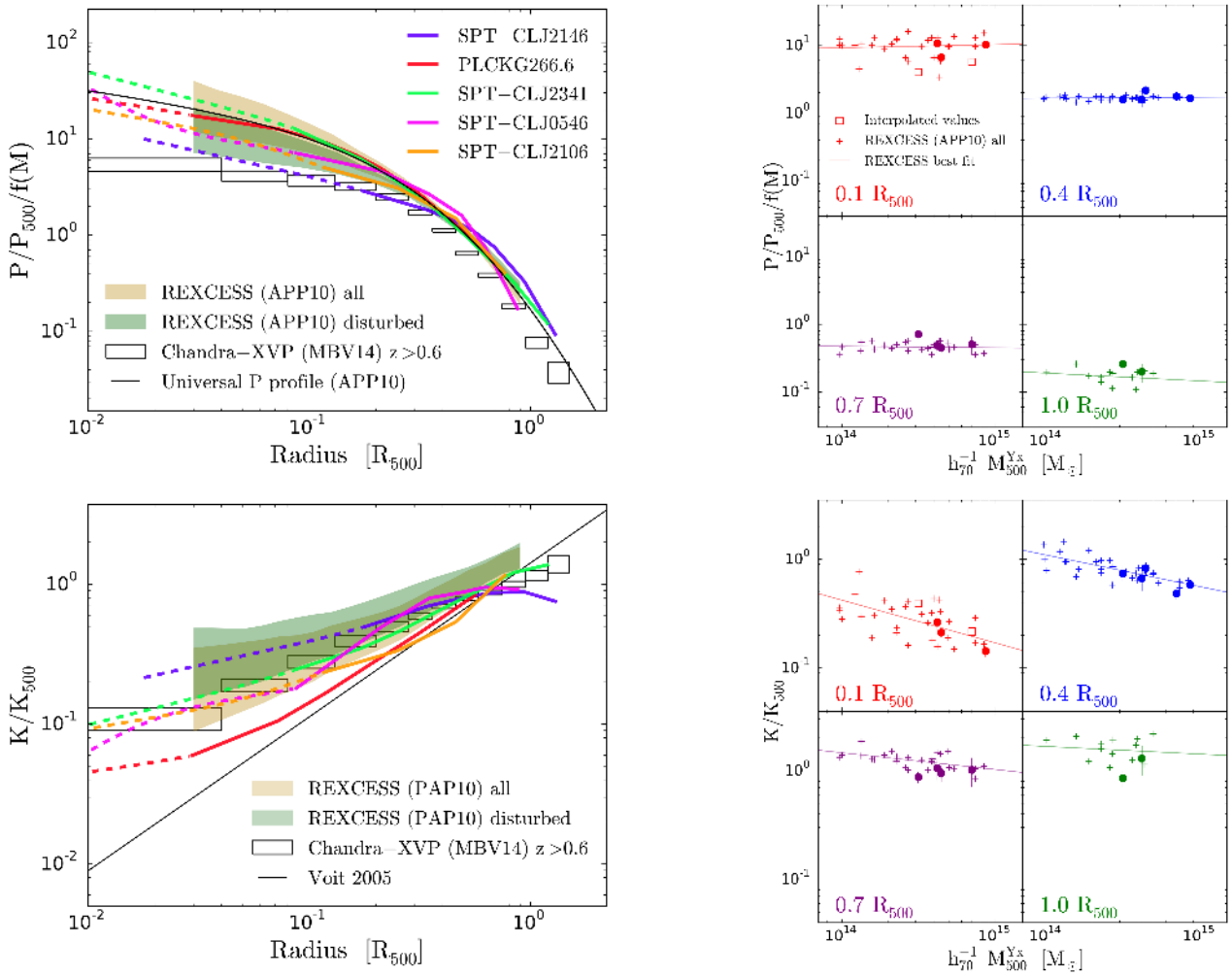

Fig. 9. *Top left*: dimensionless pressure profiles scaled by P_{500} and $f(M)$, colour-coded as in the bottom right panel of Fig. 3. The 1σ dispersion in the REXCESS pressure profiles (Arnaud et al. 2010, APP10) considering the full sample and the disturbed susbset are plotted using the same colour-code as in the left panel of Fig. 7. The black solid line is the universal pressure profile from Arnaud et al. (2010). Black boxes show the stacked pressure profile of McDonald et al. (2014, MBV14) and its uncertainty. *Top right*: scaled pressure values computed at fixed radii as a function of M_{500} of our sample (points) and REXCESS (crosses). The black solid line shows the best power-law fit to the REXCESS sample. To avoid confusion, the REXCESS errors are not plotted. *Bottom left and right*: same but for the entropy profiles, scaled by K_{500} from Pratt et al. (2010, PAP10). The black solid line shows the theoretical entropy profiles from the gravity-only simulations of Voit et al. (2005).

To investigate how the properties of our sample depends on the mass, we show in the right panel of Fig. 9 the pressure values computed at fixed radii compared to REXCESS. For each fixed radius, we fit the REXCESS sample with a power-law function of the form $Y = (N/N_0)^{\alpha}$. We show the result of the fit with a black solid line. In the inner radius panel at 0.1 R_{500}, we show the interpolated pressure profile with hollow squares. There is excellent agreement with the REXCESS best fit at 0.1, 0.4 and 0.7 R_{500}; in addition, the average deviation of the two samples is in excellent agreement. At R_{500} we have only two points, so we are not able to tell if there is a real offset.

4.4.2. Entropy profiles

In the bottom left panel of Fig. 9 we show the entropy profiles scaled by the K_{500} from Pratt et al. (2010), compared to the REXCESS 1σ dispersion envelopes. We also show the entropy profile we would expect if the structure formation were driven only by gravitational processes, as computed through simulations in Voit et al. (2005). Except for PLCK G266.6+27.3, up to $R \sim 0.4\ R_{500}$ all our of profiles are in excellent agreement with both reference samples. The entropy profile of PLCK G266.6+27.3 cluster in fact follows closely the gravity-only simulations. This is the most massive cluster in our sample and we expect that in this regime non-gravitational effects are less important; in addition, it is the only cluster that is classified as relaxed. For radii >0.5 R_{500} the profiles show lower entropy with respect to REXCESS, and flatten towards the outskirts. As discussed in McDonald et al. (2014), this behaviour may be related to gas clumpiness in the cluster outskirts (see e.g. Nagai & Lau 2011; Vazza et al. 2013). This effect boosts X-ray emission of cold gas, cooling temperature profiles in the outskirts and increasing the azimuthally averaged density profiles. We also show the entropy scaled values at fixed radii as a function of the mass in the bottom right panel of Fig. 9. As with REXCESS, we find that in the central part the most massive clusters have smaller entropy. Above 0.7 R_{500}, we clearly see the lack of entropy as compared to REXCESS. As for the scaled pressure profiles, there is good agreement in the average dispersion of our sample and that of REXCESS.

As for the density and pressure profiles, we find the same results using BCG centred profiles.

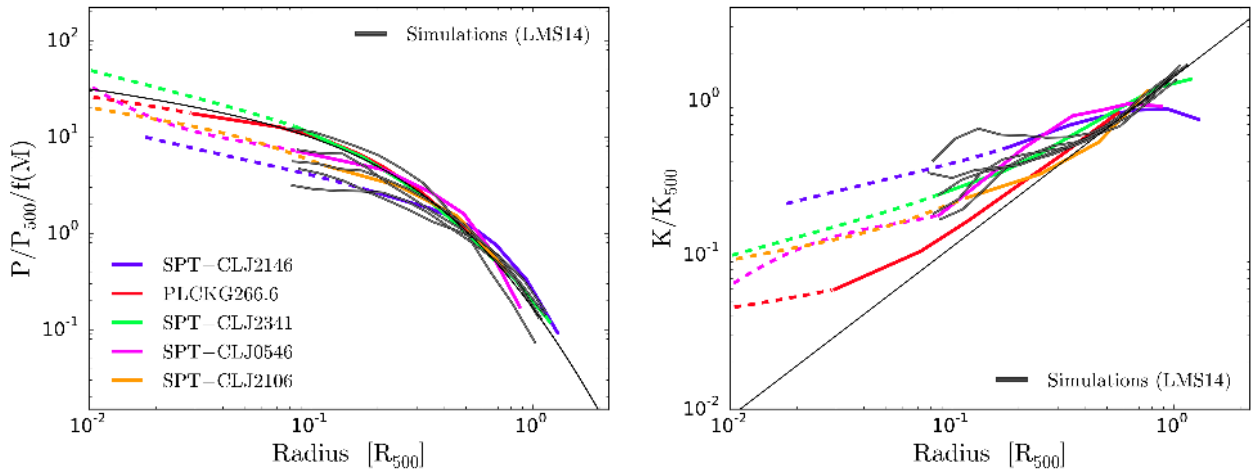

Fig. 10. *Left panel*: scaled pressure profiles, shown using the same legend as in top left panel of Fig. 9. Grey-black lines are the profiles extracted from the simulated clusters of Le Brun et al. (2014, LMS14). *Right panel*: same as left except for the fact that we show entropy profiles.

5. Comparison with *Chandra* stacked analysis

McDonald et al. (2014) analysed the redshift evolution of 80 SPT galaxy clusters observed with *Chandra*, dividing their sample into two redshift bins, and deriving stacked profiles of temperature, pressure, and entropy centred on the large-scale X-ray centroid. They classified objects as cool-core or non-cool-core based on the cuspiness of the density profile, where half of the sample was put into each category by construction. Our morphological classification is different, being based on the $\langle w \rangle$ dynamical indicator as defined for the REXCESS local sample. As a basis for comparison to our work, we thus consider the stacked profiles of the full SPT sample in their $0.6 < z < 1.2$ redshift bin.

The stacked pressure profile from McDonald et al. (2014) is plotted with open black squares in the top left panel of Fig. 9. The agreement in shape is good, but there is a clear normalisation offset of ∼10−20% with respect to REXCESS[9] and to the present $z \sim 1$ sample. In comparing the profiles, we have to consider cross-calibration differences in temperature, as discussed by McDonald et al. (2014) when comparing their *Chandra* profiles to the REXCESS profile obtained from *XMM-Newton* data. However, the observed offset is unlikely to be due to this difference. The radius R/R_{500} scales as $T^{-0.19}$ for a slope of the $M_{500}-Y_X$ relation of 0.56, and $P/P_{500} \propto T^{0.63}$. Correcting for a maximum difference of 15% in temperature (Martino et al. 2014; as assumed by McDonald et al. 2014), would translate the curve by −3% and +10% along the X- and Y-axis, respectively. As the pressure decreases with radius, the net effect is negligible (indeed, it would be null for a logarithmic slope of −3). The insensitivity of the scaled pressure profile to temperature calibration differences is also confirmed by the good agreement between local *Chandra* and *XMM-Newton* profiles shown in Arnaud et al. (2010). Furthermore, while the T_X values of the present sample are high (up to 10 keV), the effective cluster temperatures $(1+z)T$ are lower, around 5 keV, in a regime where the cross-calibration difference becomes negligible. We will thus neglect temperature cross-calibration differences in the following.

[9] This result is in contrast to McDonald et al., who found good agreement between their high-redshift subsample and the REXCESS profile for $R > 0.4\,R_{500}$ after correction for cross-calibration differences. From their Fig. 10, we suspect that this may be due to a sign error in the P/P_{500} correction.

As discussed in McDonald et al. (2014), the profile shape can be significantly affected by the choice of centre; we note that their analysis uses the large-scale centroid, whereas ours uses the X-ray peak. As illustrated in their Fig. 6, the difference in the density profile can be large even at large radii, where the profiles centred on the centroid lie below those centred on the X-ray peak. It is thus possible that some of the offset is due to the different choice of centre. We note that we do not see this difference between the BCG- and X-ray-peak centred profiles in our sample: the distance in our case is probably smaller that that between the peak and the large-scale centroid.

The bottom left panel of Fig. 9 compares the entropy profiles. Here the agreement between the entropy profiles of our sample and the stacked result from McDonald et al. (2014) is good, taking into account the larger dispersion. Both show lower entropy with respect to REXCESS at $R > 0.5\,R_{500}$, and some evidence of flattening in the outermost radii.

6. Comparison with numerical simulations

We now turn to a comparison with cosmological hydrodynamical simulations. We selected the five galaxy clusters in the mass range $[4-6]\times10^{14}\,M_\odot$ at $z = 1$ from the cosmo-OWLS simulations described in Le Brun et al. (2014). This suite is a large-volume extension of the OverWhelmingly Large Simulations project (OWLS Schaye et al. 2010), including baryonic physics such as supernova and various levels of AGN feedback, undertaken to help improve the understanding of cluster astrophysics and non-linear structure formation and evolution.

The profiles extracted from the simulated clusters were centred on the bottom of the potential well. The objects are all disturbed according to the morphological indicator calculated from the displacement between the bottom of the potential well and the centre of the mass.

The gas and total baryon fraction at R_{500} are compared to the observed sample in Fig. 8. Although the mass range is very limited, there is no obvious mass dependence, in agreement with the conclusions of Le Brun et al. (2016). This effect likely occurs because at $z \sim 1$ clusters at fixed mass are denser, hence the energy required to expel gas from the haloes is greater. The baryonic mass fraction thus stays near the universal value (the value computed from Planck Collaboration XIII 2016, is shown with a yellow rectangle).

The simulated pressure profiles shown in the left-hand panel of Fig. 10 are in excellent agreement with the observations; in particular, the observed dispersion is very well captured over the full radial range. However, the simulated entropy profiles show much less dispersion, with all simulated profiles falling very close to the result from Voit et al. (2005) at $R > 0.4\,R_{500}$. Unlike in the observed profiles, there is no hint of flattening at large radii in the simulations. This may again point to the possible influence of clumping on the observationally derived entropy.

7. Conclusions

We have presented a spatially resolved X-ray spectroscopic analysis of the five most massive ($M_{500} > 5 \times 10^{14}$ M$_\odot$), distant ($z > 0.9$) clusters thus-far detected in SZ surveys by *Planck* and SPT. All objects were observed by both *XMM-Newton* and *Chandra*, and we have investigated in detail how best to combine the datasets. Regarding the complementarity between instruments, our main results are as follows:

- We have proposed a new technique to combine X-ray datasets that allows us to fully exploit the complementarity between the high throughput of *XMM-Newton* and the excellent angular resolution of *Chandra*. Finding that the instruments are in excellent agreement concerning flux-related measurements, we performed a joint-fit to the density profiles using a modified β model. The resulting combined density profile is constrained in the centre by *Chandra*, and in the outskirts by *XMM-Newton*.
- We investigated in detail how the choice of centre for profile extraction affects the analysis, finding that profiles centred on the X-ray peak are, as expected, more peaked than when centred on the BCG. This difference is significant in the core, $R < 0.1\,R_{500}$, but it does not affect profile shape or normalisation in the outer parts of the clusters. Temperature profiles are unaffected by the choice of centre owing to the need for larger bin sizes to build and fit a spectrum.
- We find that a combination of the two instruments is fundamental for a correct determination of the cluster morphology through the centroid-shift parameter $\langle w \rangle$. At these redshifts, the high resolution of *Chandra* is essential to remove contamination from point sources. At the same time, the high throughput of *XMM-Newton* gives increased photon statistics and is critical for the detection of faint emission from substructures at large radii.

We then investigated evolution through comparison with the local X-ray selected sample REXCESS and find the following:

- Using the centroid shift parameter $\langle w \rangle$ as a morphological indicator, we find that our sample is dominated by morphologically disturbed clusters with $\langle w \rangle > 0.01$. This result is in line with expectations based on theory, where numerical simulations indicate that higher redshift objects are more likely to be undergoing mergers.
- Scaling the density profiles according to self-similar predictions, we find no clear evidence for evolution. Four of the five objects have lower central densities than the mean REXCESS profile. This is expected from the centroid shift results above, and with the expectation that disturbed cluster density profiles are flatter in the central part.
- We measured the gas-mass profiles and found good agreement with the REXCESS sample once the appropriate scaling had been applied. Combining these measurements with stellar mass measurements from the literature allowed us to measure the total baryon-mass and baryon-mass fraction. At R_{500}, we found a baryon mass fraction close to that expected from Planck Collaboration XIII (2016). There is no mass dependence, although this is likely due to the limited mass range of our sample.
- We find no clear sign of evolution in the scaled temperature profiles, the mean profile of our sample being in excellent agreement with that of REXCESS.
- The scaled pressure profiles are also in good agreement with REXCESS, within the dispersion, across the full radial range. We do not find any clear sign of evolution, either in shape or scatter, which is a fundamental result for any SZ survey that uses a detection algorithm that relies on the universality of the pressure profile.
- The scaled entropy profiles, as well as the scatter, are in good agreement with the mean REXCESS profile and its 1σ dispersion interior to $0.7\,R_{500}$. However, at larger radii there appears to be lower entropy compared to the local sample, which may be related to increased gas clumping.

We compared our results to the *Chandra* stacked analysis of SPT SZ-selected clusters at $z > 0.6$ (McDonald et al. 2014), finding good agreement in entropy behaviour but a slight normalisation offset (~10%) in pressure. Finally, we compared to the five clusters in the same mass and redshift range as our sample from the cosmo-OWLS simulations (Le Brun et al. 2014). The shape and scatter of the pressure profiles is well reproduced by the simulations. However, while the central entropy of the simulated clusters approximates the scatter in the observed profiles, beyond $R \gtrsim 0.5\,R_{500}$ the simulated entropy profiles exhibit remarkably little scatter.

Overall, our results illustrate the benefit of spatially resolved analysis of individual objects at high-redshift. This approach is fundamental to infer the statistical properties of the profiles, and in particular the dispersion around the mean. The current sample of five objects already gives a strong constraint on the mean profile and a first idea of its scatter. However, the latter is very sensitive to the number of clusters and to the presence of outliers. Deep observations of a larger number of objects will allow us to place quantitative constraints on the profile scatter. In parallel, for better comparison with theory, numerical simulations with sufficient volume to generate similarly high-mass, high-redshift samples are needed.

Acknowledgements. The authors would like to thank Amandine Le Brun and Ian McCarthy for providing the simulation data in electronic format, and Paula Tarrío for helpful comments and suggestions. The authors further thank the anonymous referee for constructive comments. This work is based in part on observations made with the *Spitzer* Space Telescope, which is operated by the Jet Propulsion Laboratory, California Institute of Technology under a contract with NASA. Based on observations made with the NASA/ESA *Hubble* Space Telescope, obtained from the data archive at the Space Telescope Science Institute. STScI is operated by the Association of Universities for Research in Astronomy, Inc. under NASA contract NAS 5-26555. The scientific results reported in this article are based on data obtained from the *Chandra* Data Archive and observations obtained with *XMM-Newton*, an ESA science mission with instruments and contributions directly funded by ESA Member States and NASA. The research leading to these results has received funding from the European Research Council under the European Union's Seventh Framework Programme (FP72007-2013) ERC grant agreement No. 340519. P.M. acknowledges funding support from NASA grant GO2-13153X.

References

Allen, S. W., Schmidt, R. W., Ebeling, H., Fabian, A. C., & van Speybroeck, L. 2004, MNRAS, 353, 457
Angulo, R. E., Springel, V., White, S. D. M., et al. 2012, MNRAS, 426, 2046

Arnaud, M., Neumann, D. M., Aghanim, N., et al. 2001, A&A, 365, L80
Arnaud, M., Pratt, G. W., Piffaretti, R., et al. 2010, A&A, 517, A92
Bartalucci, I., Mazzotta, P., Bourdin, H., & Vikhlinin, A. 2014, A&A, 566, A25
Bleem, L. E., Stalder, B., de Haan, T., et al. 2015, ApJS, 216, 27
Böhringer, H., Schuecker, P., Pratt, G. W., et al. 2007, A&A, 469, 363
Chiu, I., Mohr, J., McDonald, M., et al. 2016, MNRAS, 455, 258
Croston, J. H., Arnaud, M., Pointecouteau, E., & Pratt, G. W. 2006, A&A, 459, 1007
Croston, J. H., Pratt, G. W., Böhringer, H., et al. 2008, A&A, 487, 431
Donahue, M., Voit, G. M., Mahdavi, A., et al. 2014, ApJ, 794, 136
Freeman, P. E., Kashyap, V., Rosner, R., & Lamb, D. Q. 2002, ApJS, 138, 185
Fruscione, A., McDowell, J. C., Allen, G. E., et al. 2006, in Society of Photo-Optical Instrumentation Engineers (SPIE) Conference Series, Proc. SPIE, 6270, 62701V
Garmire, G. P., Bautz, M. W., Ford, P. G., Nousek, J. A., & Ricker, Jr., G. R. 2003, in X-Ray and Gamma-Ray Telescopes and Instruments for Astronomy., eds. J. E. Truemper, & H. D. Tananbaum, Proc. SPIE, 4851, 28
Ghizzardi, S. 2001, XMM-SOC-CAL-TN-0022
Giacconi, R., Rosati, P., Tozzi, P., et al. 2001, ApJ, 551, 624
Gottlöber, S., Klypin, A., & Kravtsov, A. V. 2001, ApJ, 546, 223
Hopkins, P. F., Croton, D., Bundy, K., et al. 2010, ApJ, 724, 915
Kaastra, J. S. 1992, An X-Ray Spectral Code for Optically Thin Plasmas, Internal SRON-Leiden Report, updated version 2.0
Kalberla, P. M. W., Burton, W. B., Hartmann, D., et al. 2005, A&A, 440, 775
Kravtsov, A. V., Vikhlinin, A., & Nagai, D. 2006, ApJ, 650, 128
Kuntz, K. D., & Snowden, S. L. 2000, ApJ, 543, 195
Kuntz, K. D., & Snowden, S. L. 2008, A&A, 478, 575
Le Brun, A. M. C., McCarthy, I. G., Schaye, J., & Ponman, T. J. 2014, MNRAS, 441, 1270
Le Brun, A. M. C., McCarthy, I. G., Schaye, J., & Ponman, T. J. 2016, MNRAS, submitted [arXiv:1606.04545]
Liedahl, D. A., Osterheld, A. L., & Goldstein, W. H. 1995, ApJ, 438, L115
Lumb, D. H., Warwick, R. S., Page, M., & De Luca, A. 2002, A&A, 389, 93
Mantz, A. B., Allen, S. W., Morris, R. G., et al. 2014, MNRAS, 440, 2077
Markevitch, M. 2010, http://cxc.cfa.harvard.edu/contrib/maxim/
Marriage, T. A., Acquaviva, V., Ade, P. A. R., et al. 2011, ApJ, 737, 61
Martino, R., Mazzotta, P., Bourdin, H., et al. 2014, MNRAS, 443, 2342
Maughan, B. J., Jones, C., Forman, W., & Van Speybroeck, L. 2008, ApJS, 174, 117
Mazzotta, P., Rasia, E., Moscardini, L., & Tormen, G. 2004, MNRAS, 354, 10
McDonald, M., Benson, B. A., Vikhlinin, A., et al. 2014, ApJ, 794, 67
Mewe, R., Gronenschild, E. H. B. M., & van den Oord, G. H. J. 1985, A&AS, 62, 197
Mewe, R., Lemen, J. R., & van den Oord, G. H. J. 1986, A&AS, 65, 511
Mohr, J. J., Fabricant, D. G., & Geller, M. J. 1993, ApJ, 413, 492
Morrison, R., & McCammon, D. 1983, ApJ, 270, 119
Nagai, D., & Lau, E. T. 2011, ApJ, 731, L10
Pen, U.-L. 1997, New Astron., 2, 309
Planck Collaboration VIII. 2011, A&A, 536, A8
Planck Collaboration XXVI. 2011, A&A, 536, A26
Planck Collaboration XXXII. 2015, A&A, 581, A14
Planck Collaboration XIII. 2016, A&A, 594, A13
Planck Collaboration XXVII. 2016, A&A, 594, A27
Pratt, G. W., & Arnaud, M. 2002, A&A, 394, 375
Pratt, G. W., Böhringer, H., Croston, J. H., et al. 2007, A&A, 461, 71
Pratt, G. W., Croston, J. H., Arnaud, M., & Böhringer, H. 2009, A&A, 498, 361
Pratt, G. W., Arnaud, M., Piffaretti, R., et al. 2010, A&A, 511, A85
Reichardt, C. L., Stalder, B., Bleem, L. E., et al. 2013, ApJ, 763, 127
Rosati, P., Tozzi, P., Gobat, R., et al. 2009, A&A, 508, 583
Santos, J. S., Tozzi, P., Rosati, P., Nonino, M., & Giovannini, G. 2012, A&A, 539, A105
Sasaki, S. 1996, PASJ, 48, L119
Schaye, J., Dalla Vecchia, C., Booth, C. M., et al. 2010, MNRAS, 402, 1536
Schellenberger, G., Reiprich, T. H., Lovisari, L., Nevalainen, J., & David, L. 2015, A&A, 575, A30
Snowden, S. L., Freyberg, M. J., Plucinsky, P. P., et al. 1995, ApJ, 454, 643
Starck, J.-L., Murtagh, F., & Bijaoui, A. 1998, Image Processing and Data Analysis: The Multiscale Approach (New York: Cambridge University Press)
Strüder, L., Briel, U., Dennerl, K., et al. 2001, A&A, 365, L18
Sunyaev, R. A., & Zeldovich, I. B. 1980, ARA&A, 18, 537
Tozzi, P., Santos, J. S., Jee, M. J., et al. 2015, ApJ, 799, 93
Turner, M. J. L., Abbey, A., Arnaud, M., et al. 2001, A&A, 365, L27
Vazza, F., Eckert, D., Simionescu, A., Brüggen, M., & Ettori, S. 2013, MNRAS, 429, 799
Vikhlinin, A. 2006, ApJ, 640, 710
Vikhlinin, A., Kravtsov, A., Forman, W., et al. 2006, ApJ, 640, 691
Voit, G. M., Kay, S. T., & Bryan, G. L. 2005, MNRAS, 364, 909

Appendix A: Gallery

In Fig. A.1 we show the *XMM-Newton* and *Chandra* images of the clusters in our sample in the left and right column, respectively. In the left-hand images, the white circle is R_{500} and the black box is the field of view of the *Chandra* image on the right. The substructures in the SPT-CLJ 2146-4632 and SPT-CLJ 0546-5345 *XMM-Newton* images are highlighted with blue dotted circles. It is worth noting that all the other sources not highlighted are consistent with being point sources. They are removed from the calculation of $\langle w \rangle$. For the sake of clarity we note that in the SPT-CLJ 2146-4632 *XMM-Newton* image a point source resolved by *Chandra* superimposes on the substructure diffuse emission.

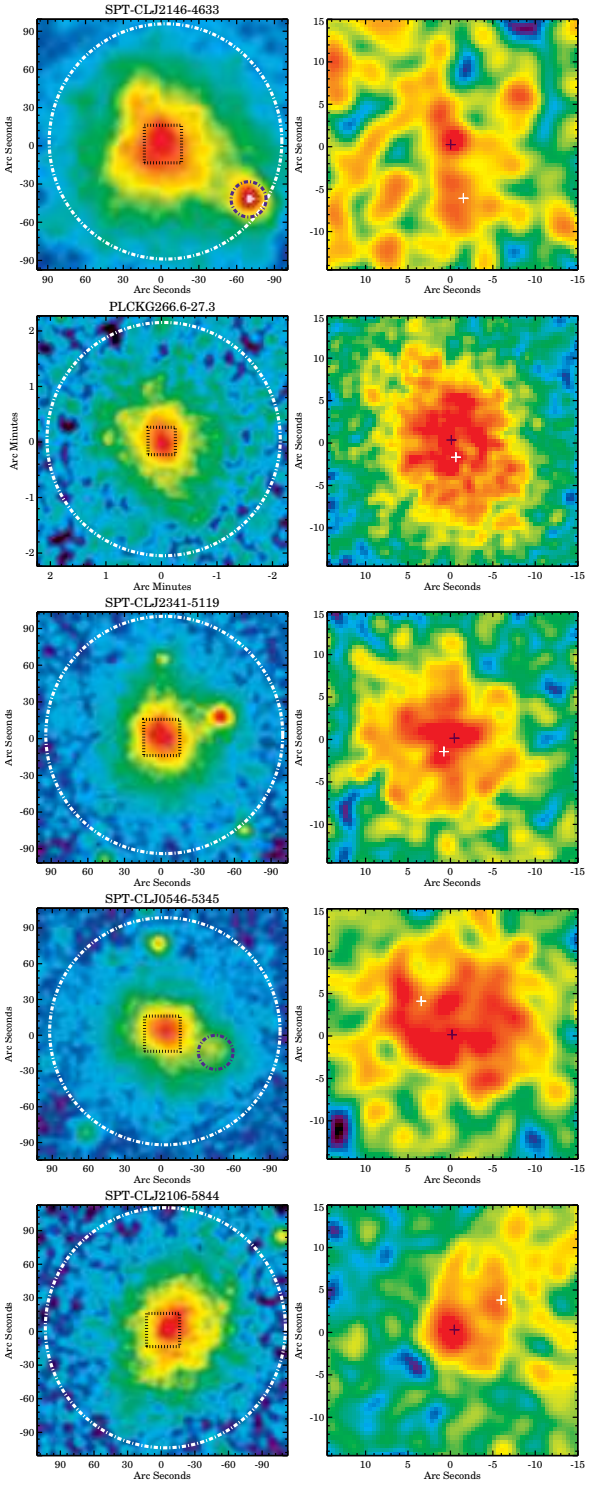

Fig. A.1. *Left column*: *XMM-Newton* images in the [0.3−2] keV band. Each image is smoothed to enhance the emission on large scale. The white dotted circle represents R_{500} and the black dotted box represents the field of view of the *Chandra* image on the right column. The blue dotted circle in the SPT-CLJ 2146-4632 and SPT-CLJ 0546-5345 images highlights the substructures. *Right column*: *Chandra* images in the [0.5−2.5] keV band. Black and white crosses identify the X-ray peak and the BCG position, respectively.

Appendix B: BCG profiles

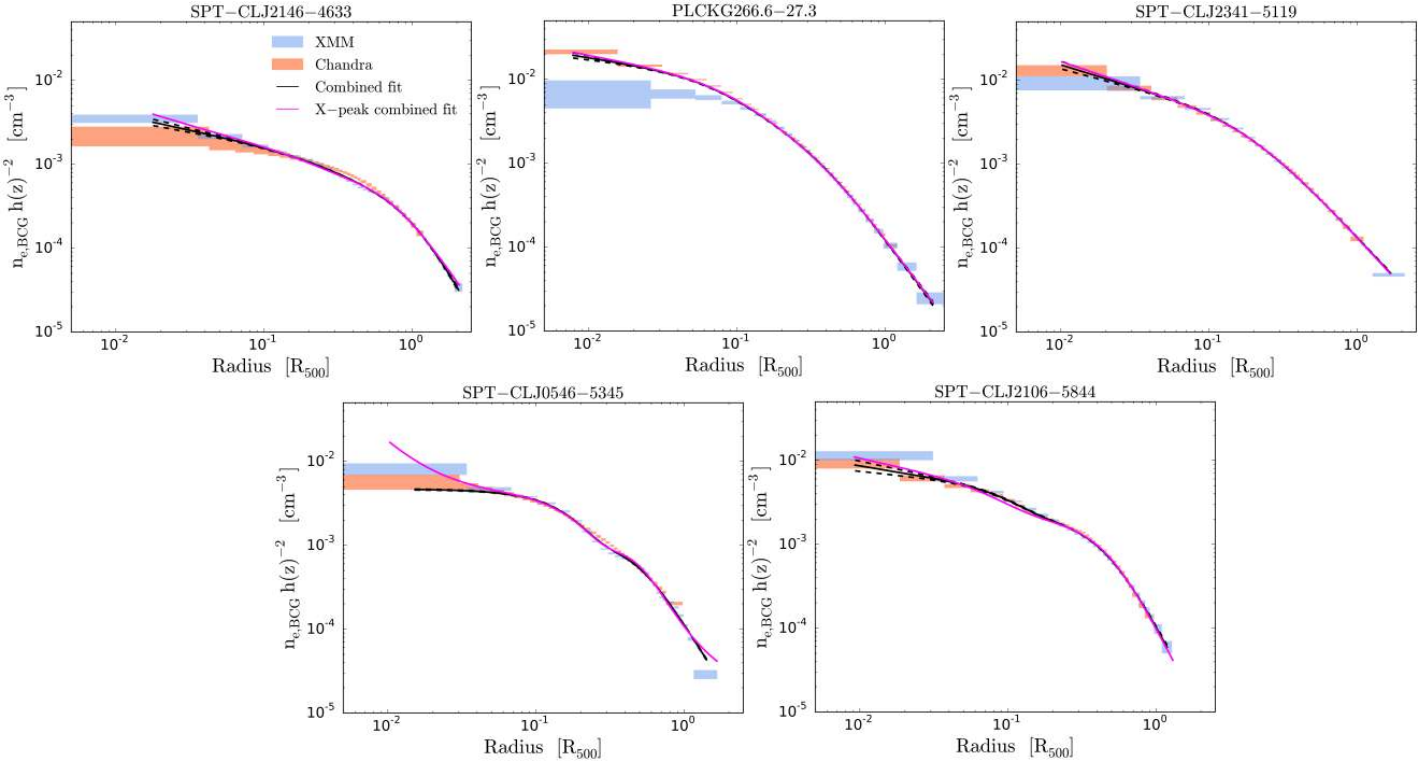

Fig. B.1. Same as Fig. 2 except that deprojected density profiles are here shown centred on the BCG.